Review of Scientific Instruments

Reconstructing 3D asymmetries in laser-direct-drive implosions on OMEGA

Cite as: Rev. Sci. Instrum. **92**, 033529 (2021); https://doi.org/10.1063/5.0043514
Submitted: 08 January 2021 . Accepted: 24 February 2021 . Published Online: 11 March 2021

O. M. Mannion, K. M. Woo, A. J. Crilly, C. J. Forrest, J. A. Frenje, M. Gatu Johnson, V. Yu. Glebov, J. P. Knauer, Z. L. Mohamed, M. H. Romanofsky, C. Stoeckl, W. Theobald, and S. P. Regan

Review of Scientific Instruments ARTICLE scitation.org/journal/rsi

Reconstructing 3D asymmetries in laser-direct-drive implosions on OMEGA

Cite as: Rev. Sci. Instrum. 92, 033529 (2021); doi: 10.1063/5.0043514
Submitted: 8 January 2021 • Accepted: 24 February 2021 •
Published Online: 11 March 2021

O. M. Mannion,[1,a)] K. M. Woo,[1] A. J. Crilly,[2] C. J. Forrest,[1] J. A. Frenje,[3] M. Gatu Johnson,[3] V. Yu. Glebov,[1] J. P. Knauer,[1] Z. L. Mohamed,[1] M. H. Romanofsky,[1] C. Stoeckl,[1] W. Theobald,[1] and S. P. Regan[1]

AFFILIATIONS

[1] Laboratory for Laser Energetics, University of Rochester, Rochester, New York 14623, USA
[2] Centre for Inertial Fusion Studies, The Blackett Laboratory, Imperial College, London SW72AZ, United Kingdom
[3] Massachusetts Institute of Technology, Plasma Science and Fusion Center, Cambridge, Massachusetts 02139, USA

Note: Paper published as part of the Special Topic on Proceedings of the 23rd Topical Conference on High-Temperature Plasma Diagnostics.
[a)] **Author to whom correspondence should be addressed:** omann@lle.rochester.edu

ABSTRACT

Three-dimensional reconstruction algorithms have been developed, which determine the hot-spot velocity, hot-spot apparent ion temperature distribution, and fuel areal-density distribution present in laser-direct-drive inertial confinement fusion implosions on the OMEGA laser. These reconstructions rely on multiple independent measurements of the neutron energy spectrum emitted from the fusing plasma. Measurements of the neutron energy spectrum on OMEGA are made using a suite of quasi-orthogonal neutron time-of-flight detectors and a magnetic recoil spectrometer. These spectrometers are positioned strategically around the OMEGA target chamber to provide unique 3D measurements of the conditions of the fusing hot spot and compressed fuel near peak compression. The uncertainties involved in these 3D reconstructions are discussed and are used to identify a new nTOF diagnostic line of sight, which when built will reduce the uncertainty in the hot-spot apparent ion temperature distribution from 700 to <400 eV.

I. INTRODUCTION

In laser-direct-drive[1] inertial confinement fusion (ICF)[2] experiments performed at the OMEGA laser,[3] an ~1- to 2-ns laser pulse is used to irradiate an ~500-μm-radius spherical capsule filled with a deuterium–tritium (DT) gas that is surrounded by a thin (~50-μm) DT ice layer. As the laser irradiates the target, it begins to implode. As the target implodes, the DT hot-spot plasma is compressed and heated to the high densities (~5 g/cm^3) and temperatures (~4 keV) required for thermonuclear fusion to occur. The laser-direct-drive experiments being performed on the OMEGA laser seek to demonstrate a hydrodynamically efficient implosion, which, if performed at a higher-energy laser facility, would achieve the conditions required for thermonuclear ignition.

Targets that are compressed asymmetrically will not fully convert their shell kinetic energy to hot-spot thermal energy, reducing the overall fusion yield generated from the implosion and decreasing the hydrodynamic efficiency of the implosion.[4,5] It is, therefore, important to minimize all perturbation sources present in the laser and target that may lead to an asymmetric compression of the target. In order to understand the impact that known perturbations have on implosions and to identify unknown perturbation sources, 3D diagnostics [i.e., having three or more diagnostic lines of sight (LOSs)] are being developed that measure the conditions of the target near peak compression.

Over the past decade, a suite of neutron diagnostics has been fielded on the OMEGA laser.[6–10] These detectors are used to measure the neutron energy spectrum emitted from the ICF target near peak compression and are used to infer the total fusion yield, hot-spot apparent ion temperature, hot-spot velocity, and fuel areal density along different lines of sight. The detectors have been strategically positioned around the OMEGA target chamber such that each detector provides unique data that can be used to reconstruct the 3D conditions of the compressed target.

In this paper, we describe the detector suite that currently exists on OMEGA and the 3D reconstruction techniques that have

been developed to interpret the measured quantities. The reconstruction techniques exploit the 3D nature of the detector suite to generate a holistic view of the conditions of the hot spot and fuel near peak compression and provide new insights into the symmetry of laser-direct-drive implosions. The techniques used to reconstruct the hot-spot velocity, apparent ion temperature distribution, and areal-density distribution will be described, and the associated uncertainties will be discussed. These techniques will be demonstrated using data from an experiment with a large mode-one drive asymmetry. Finally, we determine the optimal line of sight along which an additional neutron spectrometer could be fielded on OMEGA in order to greatly reduce the uncertainties in the 3D reconstructions.

II. NEUTRON SPECTRUM EMITTED FROM AN ICF TARGET

A. Primary neutron spectrum

The primary DT and DD thermonuclear fusion reactions occurring within the hot spot at peak compression generate spectral features in the neutron energy spectrum emitted from the ICF target at ~14.028 and ~2.45 MeV, respectively. The neutron energy spectrum produced by thermonuclear fusion reactions is well described by a normal distribution with a mean and variance that depend on the local hydrodynamic conditions of the hot spot and the direction along which the neutrons are measured.[11–14]

The mean energy of the primary neutron energy spectrum measured along a direction $\hat{d}$ can be written as[11,12]

$$\langle E \rangle = E_0 + \Delta E_{\rm th}(T_{\rm i}) + \Delta E_{\rm f}(\vec{u}\cdot\hat{d}), \tag{1}$$

where the first term is the nominal energy at which neutrons are emitted in the fusion reaction and is given by $E_0 = m_1/\hat{m}Q$, where $\hat{m} = m_1 + m_{\rm n}$ is the sum of the neutron mass $m_{\rm n}$ and the mass of the second fusion product (i.e., the alpha particle m_α for DT fusion and He^3 mass m_{He^3} for DD fusion) and Q represents the energy released in the fusion reaction. The second term is the Gamow shift due to the relative kinetic energy of the reacting ions and depends on the local thermal temperature of the hot spot.[12] The third term is the Doppler shift due to the local fluid velocity $\vec{u}$ in the hot spot and depends on the measurement direction $\hat{d}$ (Refs. 15 and 13). By measuring the mean energy of the neutrons emitted from the hot spot along multiple lines of sight, the underlying hot-spot velocity and Gamow shift can be inferred.[10,16]

The variance of the primary neutron energy spectrum can be written as[17,18]

$$\langle (E - \langle E \rangle)^2 \rangle = \frac{2m_{\rm n}E_0}{\hat{m}}T_{\rm i} + 2m_{\rm n}E_0{\rm var}(\vec{u}\cdot\hat{d}), \tag{2}$$

where $T_{\rm i}$ is the local thermal ion temperature of the plasma and ${\rm var}(\vec{u}\cdot\hat{d})$ is the variance in the fluid velocities within the hot spot along the measurement direction $\hat{d}$. The first term in this equation is isotropic, while the second term depends on the measurement direction.

The fluid velocity variances in the hot spot are not known apriori, so it is common experimentally to work with the apparent ion temperature. The apparent ion temperature is inferred directly from the variance of the measured neutron energy spectrum using Eq. (2) by neglecting the contribution from the fluid velocity variance. The apparent ion temperature can be written as[18]

$$T_{\rm i}^{\rm app} = T_{\rm i} + \hat{m}{\rm var}(\vec{u}\cdot\hat{d}). \tag{3}$$

The apparent ion temperature measurement will be sensitive to flow-velocity variances in the hot spot and will be different along different lines of sight (LOSs) depending on the amount of fluid velocity variance along each LOS. Therefore, the differences in the apparent ion temperatures measured along different lines of sight can be used to gain information on the structure of the flow-velocity variances.[18] It should be noted that because of the symmetry of the velocity variance calculation, antipodal detectors will measure the same apparent ion temperature and so do not provide additional information.

B. Scattered neutron spectrum

As the primary neutrons exit the capsule, a fraction will elastically scatter off D and T present in the dense fuel layer and generate a broad scattered neutron spectrum with energies <14 MeV. The shape of the scattered neutron energy spectrum depends on the differential elastic cross section and exact configuration of the hot spot and fuel.[19,20] Assuming a point like hot spot (neutron source) and that the areal density (scattering sites) is an infinitesimally thin shell, the number of scattered neutrons Y' can be written as

$$Y' = Y_{\rm DT}\overline{\sigma}_{\rm DT}\frac{\rho R}{\overline{m}_{\rm DT}}, \tag{4}$$

where $Y_{\rm DT}$ is the total primary DT fusion yield, $\overline{\sigma}_{\rm DT}$ is the average elastic scattering cross section of 14-MeV neutrons off D and T over the energy range that is being analyzed, $\overline{m}_{\rm DT}$ is the average atomic mass of D and T in the fuel region, and ρR is the areal density. Therefore, by measuring the number of scattered neutrons along different lines of sight, the areal density along different regions of the shell can be inferred.

It should be noted that, in experiments on OMEGA, neutrons are produced throughout the ~30-μm-radius hot spot. Additionally, neutron scattering occurs within both the hot spot and the ~10-μm-thick dense fuel region. The fact that the neutron-production volume is not a point source results in the average path length traversed by neutrons as they exit the target to be greater than the radius of the target.[21] This results in the inferred areal density using Eq. (4) to be slightly larger than the hydrodynamic areal density that is calculated by $\rho R = \int_0^\infty \rho dr$ along radial trajectories. The degree with which this affects the inferred areal density is currently being studied[22] and will be the focus of the future work. Independent of the exact hot spot and shell configuration, the areal density inferred from the number of scattered neutrons using the point source model [i.e., Eq. (4)] is a meaningful quantity that is proportional to the amount of dense material in the fuel layer.

Unlike the primary neutron energy spectrum, which contains information about the hot-spot velocity and apparent ion temperature along the detector line of sight, the scattered neutron energy spectrum contains information on the areal density throughout the entire capsule. Depending on the specific region of the neutron energy spectrum being analyzed, the areal density in different regions of the capsule can be inferred.[20] This is due to the fact that

there is an exact mapping between the cosine of the neutron scattering angle and the energy of the outgoing neutron. This results in the number of scattered neutrons in a particular neutron energy range containing information on the areal density along a specific neutron scattering angle and therefore a specific region of the dense fuel. A detailed discussion of the relationship between the regions along which the areal density is inferred from the scattered neutron spectrum can be found in Refs. 23, 19, and 20.

The neutron detectors described in Sec. III infer the areal density from either the nT backscatter edge region of the neutron energy spectrum (3.5–4.0 MeV) or the forward-scattered region (9–11 MeV). The nT backscattered-inferred areal density corresponds to neutrons with an average scattering cosine of $\mu = -0.9$, while the forward-scattered-inferred areal density corresponds to an average scattering cosine of $\mu = 0.7$. This means the nT backscatter edge inferred areal density is a measure of the areal density in the region of the dense fuel opposite to the detector line of sight, while the forward-scattered-inferred areal density is a measure of the dense fuel toward the detector line of sight. The areal-density reconstruction analysis (see Sec. IV) accounts for these kinematic effects.

III. NUCLEAR SPECTROMETERS ON OMEGA

Several nuclear spectrometers have been fielded on the OMEGA laser to infer the conditions of the target near peak compression. The current detector suite on OMEGA consists of neutron time-of-flight (nTOF)[24] detectors positioned along seven different lines of sight,[10] a magnetic recoil spectrometer (MRS),[8] and two charged-particle spectrometers (CPSs).[25] These detectors have been positioned strategically around the OMEGA target chamber such that each detector provides unique information on the conditions of the target. The configuration of the nTOF and charged-particle spectrometers around the OMEGA target chamber is shown in Figs. 1 and 2, respectively.

Measurements of the neutron energy spectrum are made using the nTOF and MRS detectors, while measurements of the knock-on deuteron spectrum are made with the CPS detectors. Due to the complexity in analyzing the knock-on deuteron spectrum at the areal densities (>100 mg/cm^2) achieved in cryogenic ICF experiments,[26]

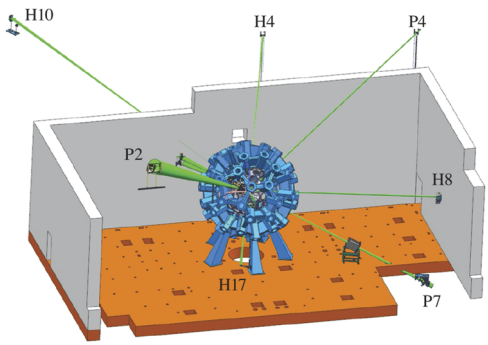

FIG. 1. Lines of sight along which neutron time-of-flight (nTOF) detectors are fielded on OMEGA. The blue structure indicates the OMEGA target chamber, while the green lines indicate the detector lines of sight.

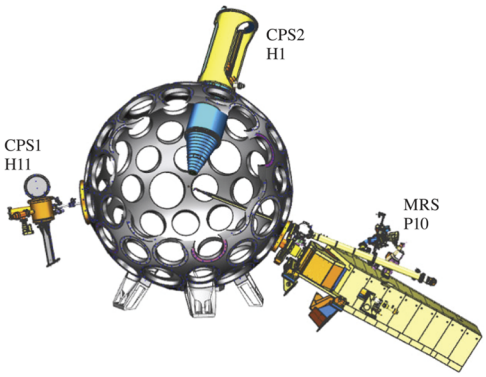

FIG. 2. Charged-particle detector suite on OMEGA, which consists of two charged-particle spectrometers (CPSs) and a magnetic recoil spectrometer (MRS). The gray structure is the OMEGA target chamber.

the CPS detectors are not currently considered in this work but will be the focus of the future work.

A. Neutron time-of-flight detectors

Neutron time-of-flight detectors measure the neutron flux arriving at a detector, located some distance away from a neutron source, as a function of time. As neutrons travel from the source to the detector, they are dispersed in time due to the spectrum of neutron energies (velocities). Neutrons with the highest energy arrive earliest in time, while lower-energy neutrons arrive later in time. By measuring the dispersion in the neutron arrival times at the detector, the neutron energy spectrum can be measured.

Several different neutron detector technologies are used on OMEGA and operate over DT fusion yields between 10^{12} and 10^{14}. Scintillator-based detectors[7,9,27] are used on OMEGA and operate by using a scintillator material to convert the neutron flux into a photon flux. This photon flux is then amplified and recorded as an electrical signal by a photomultiplier tube (PMT) that is coupled to the scintillator material. Chemical-vapor-deposition (CVD) semiconductor detectors[28] are also used on OMEGA and operate by applying a bias across a diamond and measuring the current generated by electron–hole pairs formed when the neutrons interact with the diamond material. Finally, unshielded MCP-PMT detectors[29] are used and operate by measuring the photoelectrons generated when neutrons interact with the fused-silica window of these PMT detectors.[29]

There are a total of seven nTOF detectors on OMEGA that measure the primary DT neutron spectrum. Each of these detectors measures the primary fusion yield. Six of these detectors are positioned sufficiently far from the target chamber center to provide an accurate (±200-eV) measurement of the DT apparent ion temperature.[30] Five of these detectors have been equipped with an optical timing fiducial that allows an accurate (~60 ps) absolute time-of-flight, and therefore neutron energy, measurement to be made.[10,27]

There are two nTOF detectors on OMEGA that measure both the primary DD and scattered neutron energy spectra. These detectors use an identical design[9] and are fielded in well-shielded and

collimated lines of sight. Gated PMTs are used in these detectors to avoid saturation of the detector from the large DT neutron signal. Both of these detectors are located sufficiently far from the target chamber center to measure an accurate (±200-eV) apparent DD ion temperature and are equipped with optical timing fiducials to make absolute neutron energy spectrum measurements. These detectors make high-fidelity measurements of the scattered neutron spectrum,[7] and the areal density is inferred from the nT backscattered spectral feature (3.5–4.0 MeV). As mentioned above, measurements from this region of the neutron energy spectrum can be used to infer the areal density in the region of the target opposite to the nTOF line of sight.

To infer the physical values of interest from the measured nTOF signals, a forward fit is used.[31,32] In this approach, a model neutron energy spectrum[12,22] is converted to an nTOF signal, weighted by the detector neutron sensitivity and line-of-sight attenuation, and then convolved with the detector neutron instrument response function (IRF). A least squares fit using the forward-modeled spectrum is then performed, and the optimal fit parameters are determined. The primary neutron energy spectrum analysis uses a semi-relativistic fusion neutron energy spectrum model,[12] which has a yield, apparent ion temperature, and mean neutron energy parameter. The scattered neutron energy spectrum analysis uses an analytic calculation of the scattered neutron spectrum assuming a point source and has a single areal-density parameter.[22]

The detector neutron sensitivity and line-of-sight attenuation are calculated using MCNP simulations.[31,33,34] For the primary DT neutron detectors on OMEGA, MCNP calculations show that the detector sensitivity and line-of-sight attenuation do not vary significantly across the narrow (<1-MeV) range of neutron energies analyzed by these detectors. For the primary DD and scattered neutron detectors, MCNP calculations reveal that the detector sensitivity can vary 10%–20%, while the line-of-sight attenuation can vary ~ 5% across the energy ranges that are analyzed. Therefore, in the analysis of the DD and scattered neutron spectra, the exact shape of the detector sensitivity and line-of-sight attenuation are included in the analysis.

The neutron detector instrument response function is constructed by a convolution of the detector x-ray response and the detector neutron interaction response.[31] The x-ray response is measured experimentally for each detector during calibration experiments (see discussion below). The neutron interaction response varies with neutron energy[32] and represents the different times at which neutrons generate signals within the detector. The temporal width of the neutron interaction response is dominated by the transit time of the neutrons through the detector.[32] DT neutrons are fast (~50 μm/ns) and the DT detectors on OMEGA are thin (<5 mm), resulting in the neutron interaction response being well approximated by a box function with a width <100 ps. The DD and scattered neutrons are much slower than DT neutrons, and the detectors used to measure these neutrons are 10 cm thick.[9] This results in the neutron transit time through these detectors being significant (>2 ns). The neutron interaction response has been calculated using MCNP for a variety of neutron energies.[32] In the analysis of the DD spectrum, the 2.45-MeV neutron interaction response is used, and the 3.5-MeV response is used in the scattered neutron spectrum analysis.

For the absolute time-of-flight measurements, calibration experiments are performed that generate short (<100-ps) x-ray pulses using the OMEGA or OMEGA EP lasers.[35] In these experiments, the laser irradiates a Au foil or sphere for ≤100 ps. This results in the production of a short burst of x rays, which represents a delta function for the nTOF detectors and is, therefore, a measurement of the detector x-ray response function. Furthermore, because the transit time of photons from the target to the nTOF can be calculated based on the detector distance, an absolute timing reference can be established using the x-ray signals measured with the nTOF detector.[27,36] To determine the absolute timing calibration, the delay between the expected arrival time of the x-ray to the detector distance, which is known to ~5-mm accuracy, is measured.

B. Magnetic recoil spectrometer

The MRS on OMEGA[6,8] consists of a CD_2 conversion foil placed ~10 cm from the ICF target, a large permanent magnet positioned 215 cm behind the foil, and an array of CR-39 coupons. Incident neutrons emitted from the target elastically scatter off the foil and generate recoiled deuterons. The deuterons that exit in the forward direction enter the aperture of the magnet and are spatially dispersed as they propagate through the magnetic field due to their different velocities. The deuterons are then recorded by the CR-39 coupon array, which is arranged in space such that each coupon measures deuterons at a given deflection angle (and therefore energy). Each CR-39 coupon is etched, and the deuteron yield for each deflection angle (i.e., deuteron energy) is determined.

The aperture placed in front of the magnet ensures that only near forward-scattered recoil deuterons propagate through the magnet and are recorded with the MRS detector. This ensures that there is a near one-to-one relationship between the initial energy of a neutron that interacts with the CD_2 conversion foil and the recoiled deuteron it generates. Therefore, the neutron energy spectrum can be inferred from the recoiled deuteron spectrum.

The MRS detector on OMEGA measures the primary DT neutron energy spectrum and the forward-scattered portion of the neutron energy spectrum (9–11 MeV). Due to detector resolution constraints, only the primary DT fusion yield is currently able to be accurately inferred from the primary DT spectrum.[37] The areal density is inferred by measuring the number of scattered neutrons in the 9 to 11-MeV region of the scattered neutron spectrum that corresponds to neutrons with an average scattering cosine of $\mu = 0.7$. Therefore, the MRS detector infers the areal density in the region of the target along the MRS line of sight.

To analyze the measured recoil deuteron spectrum, a forward fit is used. In this approach, a model neutron energy spectrum is propagated through the detector IRF and compared directly to the measured deuteron spectrum. The detector IRF has been simulated in Geant4[38] and accounts for the exact geometry of the detector configuration and the measured magnetic field. The IRF and absolute energy calibration are verified using calibration experiments.[8]

IV. RECONSTRUCTIONS

Each detector described in Sec. III measures either the fusion yield, apparent ion temperature, hot-spot velocity, or areal density along the detector direction. To make use of these individual

measurements, 3D reconstruction algorithms must be developed that combine the individual measurements into a holistic 3D view of the hot spot and dense fuel conditions.

In each of the reconstructions discussed below, a physics-based model is invoked that describes each measured quantity using a set of parameters. The reconstructions aim to determine the optimal parameters that best match each of the individual measurements. To accomplish this task, we assume uninformative uniform prior distributions for the model parameters and that each measurement has a normal probability distribution with a mean and variance given by the measurement value and the associated uncertainty. In this scenario, the optimal parameters can be determined by maximizing the log likelihood function[39] given by

$$\mathcal{L}(\vec{\alpha}, \{D_i\}, \sigma_i | I) = \sum_i^N \frac{(M(\vec{\alpha}|I) - D_i)^2}{\sigma_i^2}, \tag{5}$$

where $\vec{\alpha}$ is a vector of the model parameters, $M(\vec{\alpha}|I)$ is the physics model, D_i is the set of data measured along each line of sight with associated uncertainties σ_i, N is the number of measurements, and I is any external information required in the model.

In each of the reconstructions discussed below, optimization and sampling of the likelihood function was accomplished using a Markov Chain Monte Carlo (MCMC) algorithm.[40] This is convenient in that the uncertainties in the model parameters can be easily estimated using the confidence intervals of each parameter. Furthermore, the apparent ion temperature reconstruction model has six parameters that can be difficult to optimize with standard gradient decent algorithms.

The reconstruction algorithms discussed below will be applied to the measurements made on OMEGA shot 94 660. This shot was known to have a large mode-one drive asymmetry due to anomalous laser beam pointing errors.[41] This experiment is, therefore, a good candidate for testing these reconstruction algorithms since the asymmetries in the hot spot and DT fuel are exacerbated, in a known direction, and can be resolved with the current measurement uncertainties. From 3D radiation-hydrodynamic simulations, experiments with large mode-one drive asymmetries are expected to have large hot-spot flow velocities (>100 km/s) in the direction of the mode-one drive asymmetry.[4] Additionally, simulations find that a large apparent ion temperature (>1.0-keV) asymmetry and areal-density asymmetry will also be present and aligned with the hot-spot velocity and mode-one direction.[4,18,41] Therefore, we can use these experimental results to check if these reconstruction techniques are consistent with the expectation from radiation-hydrodynamic simulations.

A. Hot-spot velocity

To reconstruct the hot-spot velocity that was present in an experiment, the mean energy measurements made using the nTOF detectors are used. The physics model for the mean energy measured along a line-of-sight $\hat{d}$ of a neutron species s can be written using Eq. (1) as

$$M(\vec{\alpha}|\hat{d}, s) = E_0^s + \Delta E_{\text{th}}^s + \Delta E_{\text{f}}^s(\vec{u} \cdot \hat{d}), \tag{6}$$

with the parameters of the fit being $\vec{\alpha} = (u_x, u_y, u_z, \Delta E_{\text{th}}^{\text{DT}}, \Delta E_{\text{th}}^{\text{DD}})$. Here, u_x, u_y, u_z are the Cartesian components of the hot-spot velocity vector $\vec{u}$ and $\Delta E_{\text{th}}^{\text{DT}}$ and $\Delta E_{\text{th}}^{\text{DD}}$ are the Gamow shifts of the DT and DD fusion reactions, respectively. This model makes it explicit that the appropriate E_0, ΔE_{th}, and ΔE_{f} be used when comparing to neutron data from a specific fusion reaction. Note that, in this model, we have assumed that both species sample the hydrodynamic conditions equally. This assumption is supported by 3D radiation-hydrodynamic simulations that show only a small deviation between the production rates of DT and DD reactions in the capsule in both space and time.[42]

The dataset $\{D_i\}$ that is compared to this model is the individual mean energy measurement inferred from the primary DT and DD neutron energy spectra made with the nTOF detectors. Each of the nTOF measurements has a mean energy uncertainty between 5 and 17 keV.[10]

This model has been applied to the data of shot 94 660 on OMEGA. The hot-spot velocity reconstruction was found to have a magnitude of 155 ± 11 km/s. The direction of the velocity was in the direction $\theta = 74^\circ \pm 6^\circ$ and $\phi = 139^\circ \pm 5^\circ$ in the OMEGA coordinate system. This direction is well aligned with the direction of the known mode-one drive asymmetry,[41] which was directed along $(\theta, \phi) = (51^\circ, 122^\circ)$. The mode-one direction was determined using a hard sphere laser illumination calculation using the measured beam pointing, target offset, and laser energy in this experiment.[41] Figure 3 shows the direction of the reconstructed hot-spot velocity in the OMEGA coordinate system.

The uncertainties in the hot-spot velocity reconstruction parameters are determined from the confidence intervals of the likelihood function. The uncertainty in the hot-spot velocity magnitude is ~11 km/s, while the uncertainty in the polar angle is ~ 6° and the azimuthal angle is ~ 5°. To visualize the directional uncertainty, a separate Monte Carlo analysis was performed, in which an ensemble of synthetic neutron mean energy measurement datasets were generated using the known uncertainty of each measurement. The velocity reconstruction algorithm was then applied to these synthetic datasets, and the hot-spot velocity was determined. Figure 3 shows the ensemble of reconstructed hot-spot velocities from this Monte Carlo study. The cloud of reconstructed hot-spot velocity vectors represents the uncertainty in the hot-spot velocity direction.

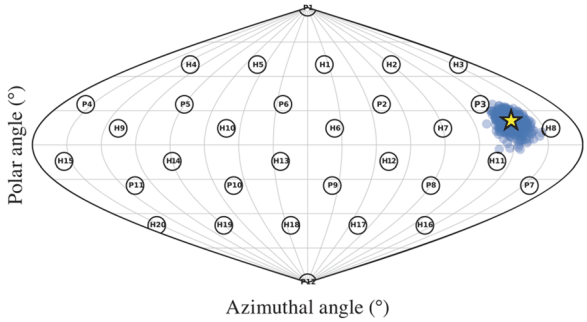

FIG. 3. A sinusoidal projection of the OMEGA target chamber coordinate system showing the reconstructed hot-spot velocity (yellow star) and the uncertainty in the direction (blue cloud) of this reconstruction determined through a Monte Carlo analysis. The diagnostic ports on OMEGA are indicated by the circles with the H and P labels.

B. Apparent ion temperature distribution

To reconstruct the apparent ion temperature distribution that was present in an experiment, the apparent ion temperature measurements made using the nTOF's are used. In the analysis presented here, only the DT apparent ion temperature measurements will be considered. The physics model for the measured apparent ion temperature along a line-of-sight $\hat{d}$ is given by Eq. (3), which can be written as

$$M(\vec{\alpha}|\hat{d}, T_{\rm th}, \hat{m}) = T_{\rm th} + \hat{m}{\rm Var}(\vec{u}\cdot\hat{d}), \tag{7}$$

with the parameters of the fit given by $\vec{\alpha} = (\sigma_{xx}^2, \sigma_{yy}^2, \sigma_{zz}^2, 2\sigma_{xy}^2, 2\sigma_{yz}^2, 2\sigma_{zx}^2)$ and representing the Cartesian components of the flow-velocity variances and covariances. For an extensive description of this model, see Ref. 18.

In order to complete this reconstruction, the thermal ion temperature $T_{\rm th}$ must be known. In this analysis, we approximate the thermal ion temperature as the minimum apparent ion temperature measured in the experiment. This limits the reconstruction to only be sensitive to the anisotropic flow-velocity variances that are present in the hot spot.[42] Other choices for the thermal ion temperature, for example, the DD apparent ion temperature or the electron temperature, will be explored in the future work.

The apparent ion temperature reconstruction has been performed for shot 94 660, and the velocity variances and covariances have been determined. The standard deviation of the reconstructed velocity variances and covariances is shown in Table I. We see that the standard deviation of the velocities within the hot spot was large (>100 km/s) on this shot. The magnitude of these values is consistent with those found in highly perturbed radiation-hydrodynamic simulations.[42] The principal eigenvector of the flow velocity covariance matrix constructed using the values in Table I is along the direction $(\theta, \phi) = (53^\circ, 135^\circ)$ and represents the direction of maximum flow velocity variance. This direction is consistent with the direction of the hot-spot velocity reconstruction in Sec. IV A.

To better understand the 3D nature of the apparent ion temperature reconstruction and to compare with the hot-spot velocity measurement, it is useful to calculate the apparent ion temperature along all directions on OMEGA using the reconstructed velocity variances (see Fig. 4, which shows the apparent ion temperature reconstruction along with the hot-spot velocity). We see that the regions of high apparent ion temperature, indicating regions of high velocity variances, are near parallel and antiparallel to the reconstructed hot-spot velocity. The apparent ion temperature asymmetry being aligned with the hot-spot velocity direction is consistent with results from radiation-hydrodynamic simulations when strong mode-one asymmetries are present.[4,18]

The uncertainty in the apparent ion temperature distribution reconstructions has been inferred from the confidence intervals of the likelihood function. The uncertainties in the standard deviation of the flow-velocity variances and covariances are between 50 and 100 km/s and are shown in Table I. Note that there is a large uncertainty in the fluid velocity variances along the z direction. This is a result of the fact that no DT apparent ion temperature detector has yet to be fielded near the north or south pole of the OMEGA target chamber. This leaves the component of the fluid velocity variances along the z direction to be the least constrained.

TABLE I. Standard deviation of the variances and covariances of the hot-spot velocity inferred from the apparent ion temperature reconstructed in km/s. Note that some of the covariance terms are negative and so require the inclusion of the imaginary number $i = \sqrt{-1}$.

$\sqrt{\sigma_{xx}^2}$	$\sqrt{\sigma_{yy}^2}$	$\sqrt{\sigma_{zz}^2}$	$\sqrt{\sigma_{xy}^2}$	$\sqrt{\sigma_{yz}^2}$	$\sqrt{\sigma_{zx}^2}$
120 ± 60	110 ± 80	150 ± 100	100i ± 50	80 ± 60	80i±50

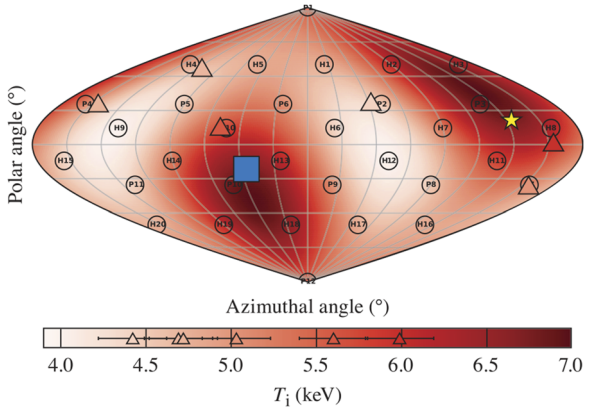

FIG. 4. A sinusoidal projection of the OMEGA target chamber coordinate system showing the reconstructed hot-spot velocity direction (yellow star), the antipodal direction of the hot-spot velocity (blue square), the measured DT apparent ion temperatures (triangles), and the apparent ion temperature reconstruction (red color map) for shot 94 660.

To guide visualization of the uncertainties in the apparent ion temperature reconstructions, a Monte Carlo study was performed where random realizations of the six DT apparent ion temperature measurements were generated using the measured value of each detector and their uncertainties. The apparent ion temperature reconstruction was performed for each of the synthetic datasets, and the predicted apparent ion temperature along each direction on OMEGA was determined. To identify the directions that have the largest uncertainties, the standard deviation of the predicted apparent ion temperature along each direction was calculated and is shown in Fig. 5. The two antipodal lines of sight along which there is the largest apparent ion temperature uncertainty have been identified. These directions are $(\theta, \phi) = (32^\circ, 123^\circ)$ and $(\theta, \phi) = (147^\circ, 303^\circ)$ and have an apparent ion temperature uncertainty of ~700 eV.

Fielding a neutron spectrometer near this direction will reduce the uncertainty in the apparent ion temperature reconstruction. The closest diagnostic port to this direction along which an additional nTOF detector can be fielded is the H2 port on OMEGA that is located along the direction $(\theta, \phi) = (37^\circ, 90^\circ)$. To calculate the uncertainties in the apparent ion temperature reconstruction if a detector is placed at the H2 LOS, the same Monte Carlo procedure was repeated, but now including a detector along the H2 LOS. The new detector was assumed to have the average uncertainty of the current detectors on OMEGA. The standard deviation of the reconstructed inferred apparent ion temperature distribution along each direction with the inclusion of this detector is shown in Fig. 6. Including a

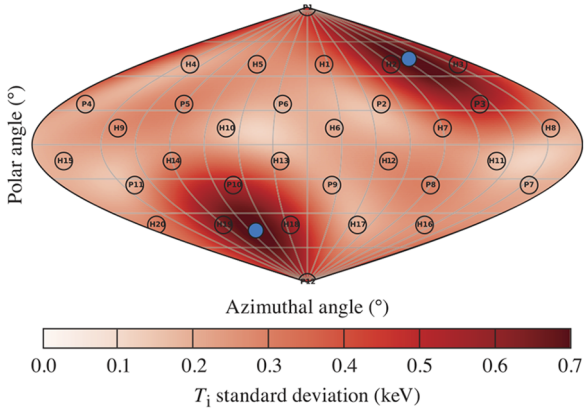

FIG. 5. A sinusoidal projection of the OMEGA target chamber coordinate system showing the uncertainty in the apparent ion temperature reconstruction using the current detector suite on OMEGA. The blue circles are the antipodal directions with the largest apparent ion temperature uncertainty.

detector along this direction is found to reduce the maximum apparent ion temperature uncertainty to <400 eV. A nTOF detector to be fielded along the H2 line of sight is currently being designed and will be included in the future analysis.

C. Areal-density distribution

To reconstruct the areal-density distribution in a given experiment, the inferred areal-density measurements from the two nTOF detectors and MRS detector on OMEGA are used. There are several different models that could be used in the areal-density reconstruction. A natural model to use, given the spherical geometry of these implosions, is a spherical harmonic decomposition of the areal-density distribution. Such a model has been developed[20] but requires at least four areal-density measurements in order to resolve even the lowest of modes (i.e., $\ell = 1$). On OMEGA, there are only three areal-density measurements currently available. Therefore, to accomplish an areal-density reconstruction with the current detector systems, external information must be included in the model to further constrain the system.

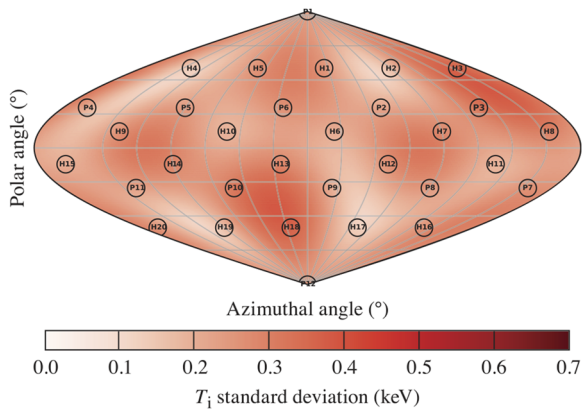

FIG. 6. A sinusoidal projection of the OMEGA target chamber coordinate system showing the uncertainty in the apparent ion temperature reconstruction if an additional detector is fielded along the H2 LOS.

It has been shown in analytic models,[43] detailed radiation-hydrodynamic simulations,[4] and experiments on the NIF[44] that there are strong correlations between the direction of the measured hot-spot velocity and the areal-density asymmetry direction. In particular, the direction of minimum areal density is expected to be along the direction of the hot-spot velocity, while the direction of maximum areal density is expected to be along the direction opposite to the hot-spot velocity. Therefore, a mode-one areal-density reconstruction model is used on OMEGA and is given by

$$M(\vec{\alpha}|\hat{d},\mu) = \rho R_0 + \Delta\rho R\ (\hat{u}\cdot\hat{d})\mu, \tag{8}$$

where $\vec{\alpha} = (\rho R_0, \Delta\rho R)$; ρR_0 is the 4 π average areal density; $\Delta\rho R$ is the variation in the areal density; $\hat{d}$ and $\hat{u}$ are the areal-density detector direction and the measured hot-spot velocity direction, respectively; and μ is the average neutron-scattering cosine associated with the region of the neutron energy spectrum from which the areal density is inferred.

The use of the hot-spot velocity measurement allows the direction of the areal-density variation to be held fixed, while the areal-density measurements from the nTOF and MRS detectors are used to determine the magnitude of the average areal density and the variation in the areal density. Due to the constraints of this model, only mode-one areal-density asymmetries can be resolved.

The areal-density reconstruction has been performed for shot 94 660, and the average areal density and areal-density variation were determined. From the reconstruction, the average 4π areal density was inferred to be $\rho R_0 = 115 \pm 9$ mg/cm^2, while the variation in the areal density was found to be $\Delta\rho R = 54 \pm 12$ mg/cm^2. The uncertainty in the areal-density reconstruction parameters ρR_0 and $\Delta\rho R$ has been inferred from the confidence intervals of the likelihood function. The uncertainty in the direction of the areal-density asymmetry is entirely determined by the uncertainty in the hot-spot velocity reconstruction discussed above.

Using the reconstruction values of ρR_0 and $\Delta\rho R$, the areal-density distribution can be visualized by calculating the areal density predicted around the OMEGA coordinate system. This areal-density reconstruction for shot 94 660 is shown in Fig. 7. The individual areal-density measurements are shown as the diamonds with the color of the diamond being related to the inferred areal density. The location at which the diamonds are shown is the location about which the areal-density measurements are made accounting for the average scattering cosine term. This means that the areal density inferred from the nTOF detectors, which are backscatter measurements, is plotted along the direction opposite to their line of sight, while the MRS detector, a forward-scatter measurement, is plotted along the LOS of the detector. From this reconstruction, we can visualize the areal-density asymmetry present in the implosion and compare with other measurements. We see that the areal-density measurements are consistent with the mode-one asymmetry observed in the apparent ion temperature reconstruction.

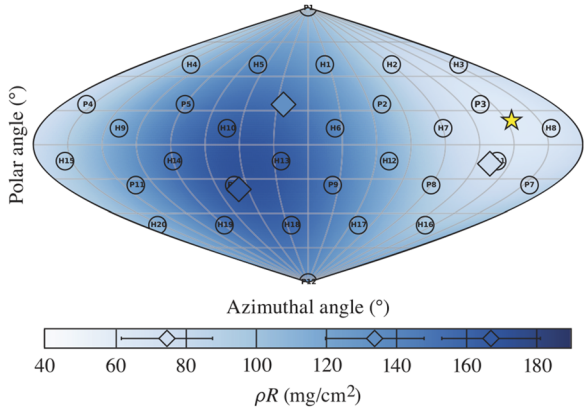

FIG. 7. A sinusoidal projection of the OMEGA target chamber coordinate system showing the reconstructed hot-spot velocity (yellow star), measured areal densities (diamonds), and areal-density reconstruction (blue color map) for shot 94 660.

V. CONCLUSIONS

Here, we have presented the neutron diagnostic suite and reconstruction techniques that are used to study 3D asymmetries in laser-direct-drive implosions on OMEGA. These techniques were demonstrated using data from an experiment with a large mode-one drive asymmetry, and the results were found to be consistent with the expectation from radiation-hydrodynamic simulations[4,18] and experimental results on the NIF.[44] The analysis of the uncertainties in the apparent ion temperature reconstruction was discussed and was used to identify the optimal line of sight to build an additional apparent ion temperature detector, which when built will reduce the error in the apparent ion temperature reconstructions to <400 eV.

Future work will focus on extending these reconstructions by incorporating more measurements. In particular, the recent theoretical work[42] has demonstrated that if the DD apparent ion temperature measurements are included in the apparent ion temperature reconstruction, the thermal ion temperature can be inferred. A more general areal-density reconstruction will be developed so that the direction of the areal-density asymmetry need not be assumed along the direction of the hot-spot velocity. This will require the inclusion of more areal-density measurements and can be obtained from the knock-on deuteron spectrum measured by the CPS detectors on OMEGA (see Fig. 2).

ACKNOWLEDGMENTS

This material is based upon the work supported by the Department of Energy National Nuclear Security Administration under Award No. DE-NA0003856, of the University of Rochester, and the New York State Energy Research and Development Authority. The support of DOE does not constitute an endorsement by DOE of the views expressed in this paper. This report was prepared as an account of work sponsored by an agency of the U.S. Government. Neither the U.S. Government nor any agency thereof, nor any of their employees, makes any warranty, express or implied, or assumes any legal liability or responsibility for the accuracy, completeness, or usefulness of any information, apparatus, product, or process disclosed, or represents that its use would not infringe privately owned rights. Reference herein to any specific commercial product, process, or service by trade name, trademark, manufacturer, or otherwise does not necessarily constitute or imply its endorsement, recommendation, or favoring by the U.S. Government or any agency thereof. The views and opinions of authors expressed herein do not necessarily state or reflect those of the U.S. Government or any agency thereof.

DATA AVAILABILITY

The data that support the findings of this study are available from the corresponding author upon reasonable request.

REFERENCES

[1] A. F. Gibson, Phys. Educ. **15**, 4 (1980).
[2] J. Nuckolls, L. Wood, A. Thiessen, and G. Zimmerman, Nature **239**, 139 (1972).
[3] T. R. Boehly *et al.*, Opt. Commun. **133**, 495 (1997).
[4] B. K. Spears *et al.*, Phys. Plasmas **21**, 042702 (2014).
[5] K. M. Woo *et al.*, Phys. Plasmas **25**, 052704 (2018).
[6] J. A. Frenje *et al.*, Phys. Plasmas **17**, 056311 (2010).
[7] C. J. Forrest *et al.*, Rev. Sci. Instrum. **83**, 10D919 (2012).
[8] D. T. Casey *et al.*, Rev. Sci. Instrum. **84**, 043506 (2013).
[9] V. Yu. Glebov, C. J. Forrest, K. L. Marshall, M. Romanofsky, T. C. Sangster, M. J. Shoup, and C. Stoeckl, Rev. Sci. Instrum. **85**, 11E102 (2014).
[10] O. M. Mannion *et al.*, Nucl. Instrum. Methods Phys. Res., Sect. A **964**, 163774 (2020).
[11] H. Brysk, Plasma Phys. **15**, 611 (1973).
[12] L. Ballabio, J. Källne, and G. Gorini, Nucl. Fusion **38**, 1723 (1998).
[13] B. Appelbe and J. Chittenden, Plasma Phys. Controlled Fusion **53**, 045002 (2011).
[14] D. H. Munro, Nucl. Fusion **56**, 036001 (2016).
[15] T. J. Murphy, Phys. Plasmas **21**, 072701 (2014).
[16] R. Hatarik, R. C. Nora, B. K. Spears, M. J. Eckart, G. P. Grim, E. P. Hartouni, A. S. Moore, and D. J. Schlossberg, Rev. Sci. Instrum. **89**, 10I138 (2018).
[17] T. J. Murphy, R. E. Chrien, and K. A. Klare, Rev. Sci. Instrum. **68**, 614 (1997).
[18] K. M. Woo *et al.*, Phys. Plasmas **25**, 102710 (2018).
[19] A. J. Crilly, B. D. Appelbe, K. McGlinchey, C. A. Walsh, J. K. Tong, A. B. Boxall, and J. P. Chittenden, Phys. Plasmas **25**, 122703 (2018).
[20] A. J. Crilly, B. D. Appelbe, O. M. Mannion, C. J. Forrest, and J. P. Chittenden, "The effect of areal density asymmetries on scattered neutron spectra in ICF implosions," Phys. Plasmas **28**, 022710 (2021).
[21] G. P. Grim *et al.*, Phys. Plasmas **20**, 056320 (2013).
[22] Z. L. Mohamed, O. M. Mannion, J. P. Knauer, C. J. Forrest, V. Yu. Glebov, and C. Stoeckl, "Application of an energy-dependent instrument response function to analysis of nTOF data from cryogenic DT experiments," Rev. Sci. Instrum. (to be published).
[23] M. Gatu Johnson *et al.*, Rev. Sci. Instrum. **83**, 10D308 (2012).
[24] R. A. Lerche, L. W. Coleman, J. W. Houghton, D. R. Speck, and E. K. Storm, Appl. Phys. Lett. **31**, 645 (1977).
[25] D. G. Hicks, Ph.D. thesis, Massachusetts Institute of Technology, 1999.
[26] J. A. Frenje, C. K. Li, F. H. Séguin, D. T. Casey, R. D. Petrasso, T. C. Sangster, R. Betti, V. Yu. Glebov, and D. D. Meyerhofer, Phys. Plasmas **16**, 042704 (2009).
[27] O. M. Mannion, V. Yu. Glebov, C. J. Forrest, J. P. Knauer, V. N. Goncharov, S. P. Regan, T. C. Sangster, C. Stoeckl, and M. Gatu Johnson, Rev. Sci. Instrum. **89**, 10I131 (2018).
[28] G. J. Schmid *et al.*, Rev. Sci. Instrum. **74**, 1828 (2003).
[29] V. Yu. Glebov, C. Stoeckl, C. J. Forrest, J. P. Knauer, O. M. Mannion, M. H. Romanofsky, T. C. Sangster, and S. P. Regan, Rev. Sci. Instrum. **92**, 013509 (2021).
[30] R. A. Lerche and B. A. Remington, Rev. Sci. Instrum. **61**, 3131 (1990).

[31] R. Hatarik *et al.*, J. Appl. Phys. **118**, 184502 (2015).
[32] Z. L. Mohamed, O. M. Mannion, E. P. Hartouni, J. P. Knauer, and C. J. Forrest, J. Appl. Phys. **128**, 214501 (2020).
[33] C. J. Forrest *et al.*, Nucl. Instrum. Methods Phys. Res., Sect. A **888**, 169 (2018).
[34] T. Goorley *et al.*, Nucl. Technol. **180**, 298 (2012).
[35] C. Stoeckl *et al.*, Rev. Sci. Instrum. **87**, 053501 (2016).
[36] R. A. Lerche, D. R. Kania, S. M. Lane, G. L. Tietbohl, C. K. Bennett, and G. P. Baltzer, Rev. Sci. Instrum. **59**, 1697 (1988).
[37] M. Gatu Johnson *et al.*, Rev. Sci. Instrum. **89**, 10I129 (2018).
[38] S. Agostinelli *et al.*, Nucl. Instrum. Methods Phys. Res., Sect. A **506**, 250 (2003).
[39] G. Cowan, Statistical Data Analysis (Clarendon Press, 1998), p. 197.
[40] D. Foreman-Mackey, D. W. Hogg, D. Lang, and J. Goodman, Publ. Astron. Soc. Pac. **125**, 306 (2013).
[41] O. M. Mannion *et al.*, "Mitigation of mode-one asymmetry in laser-direct-drive inertial confinement fusion implosions," Phys. Plasmas (submitted).
[42] K. M. Woo *et al.*, Phys. Plasmas **27**, 062702 (2020).
[43] O. A. Hurricane *et al.*, Phys. Plasmas **27**, 062704 (2020).
[44] H. G. Rinderknecht, D. T. Casey, R. Hatarik, R. M. Bionta, B. J. MacGowan, P. Patel, O. L. Landen, E. P. Hartouni, and O. A. Hurricane, Phys. Rev. Lett. **124**, 145002 (2020).